Journal of Materials Science & Technology 35 (2019) 777–783

Contents lists available at ScienceDirect

Journal of Materials Science & Technology

journal homepage: www.jmst.org

Research Article

Effect of grain refinement and crystallographic texture produced by friction stir processing on the biodegradation behavior of a Mg-Nd-Zn alloy

Wen Zhang[a], Lili Tan[b,*], Dingrui Ni[b], Junxiu Chen[b], Ying-Chao Zhao[a], Long Liu[a], Cijun Shuai[a], Ke Yang[b], Andrej Atrens[c], Ming-Chun Zhao[a,*]

[a] School of Material Science and Engineering, Central South University, Changsha, 410083, China
[b] Institute of Metal Research, Chinese Academy of Sciences, Shenyang, 110016, China
[c] Division of Materials, The University of Queensland, Brisbane, Qld, 4072, Australia

ARTICLE INFO

Article history:
Received 8 September 2018
Received in revised form 19 October 2018
Accepted 1 November 2018
Available online 27 November 2018

Keywords:
Mg alloy
Friction stir processing
Grain refinement
Texture evolution
Biodegradation

ABSTRACT

The application of a single pass of friction stir processing (FSP) to Mg-Nd-Zn alloy resulted in grain refinement, texture evolution and redistribution of second phases, which improved corrosion resistance. In this work, an as-rolled Mg-Nd-Zn alloy was subjected to FSP. The microstructure in the processed zone of the FS-400 rpm alloy exhibited refined grains, a more homogenous grain size distribution, less second phases, and stronger basal plane texture. The corrosion behavior assessed using immersion tests and electrochemical tests in Hank's solution indicated that the FS-400 rpm alloy had a lower corrosion rate, which was attributed to the increase of basal plane intensity and grain refinement. The hardness was lowered slightly and the elongation was increased, which might be attributed to the redistribution of the crushed second phases.

1. Introduction

Mg alloys are a class of new biomedical metal materials [1–5]. Mg alloy implants can degrade gradually in the body fluids until they eventually disappear [3,2–5]. Compared to currently biodegradable polymeric materials, Mg alloys can provide adequate strength for the time of body repair and still retain the advantage of metallic materials [6–8]. However the control of the degradation rate of Mg alloys in physiological environment is still a big challenge. So far, it is still difficult for Mg alloys to meet the requirements of the degradation rate [9–12]. Recently, thermo-mechanical processing was used to decrease the corrosion rate of Mg alloys by grain refinement. Aung and Zhou [13] found that the corrosion rate in 3.5 wt% NaCl solution of AZ31B decreased for a smaller grain size. Similarly, Birbilis et al. [14] reported that grain refinement decreased the corrosion rate of pure Mg in 0.1 M NaCl solution. Argade et al. [15] and Alvarez-Lopez et al. [16] suggested that grain boundaries acted as a barrier of corrosion to retard the progress of corrosion.

Friction stir processing (FSP) is a new thermo-mechanical processing technique, which can modify alloy microstructures by using a non-consumable rotating tool consisting of shoulder and pin [17]. The FSP grain refinement mechanism has been elucidated [18]. Furthermore, FSP has been shown to improve the corrosion resistance by the grain refinement. For example, Arora et al. [19] found that FSP decreased the corrosion rate of AE42 in 3.5 wt% NaCl solution. Similarly, Argade et al. [20] demonstrated that FSP decreased the corrosion rate of Mg-Y-RE in 3.5 wt% NaCl solution. However, the above-mentioned research was concentrated on grain refinement and ignored the other significant microstructural changes, especially the texture and the redistribution of secondary phases. This current work carried out a comprehensive study of the influence of grain size, texture and redistribution of second phases on the corrosion behavior of Mg-Nd-Zn subjected to a friction stir processing. This work studied the evolution of microstructure, macro-texture, mechanical properties, re-distribution of intermetallic particles, electrochemical behavior, and immersion performance.

* Corresponding authors.
E-mail addresses: lltan@imr.ac.cn (L. Tan), mczhao@csu.edu.cn (M.-C. Zhao).

https://doi.org/10.1016/j.jmst.2018.11.025
1005-0302/

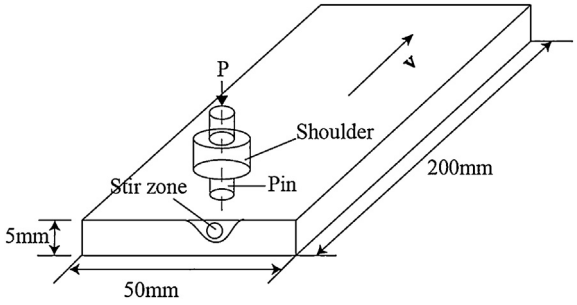

Fig. 1. Schematic of friction stir processing.

2. Experiments and methods

2.1. As-received material

The cast ingot of Mg-2Nd-0.2 Zn alloy (designated as NZ20) was preheated at 350 °C for 2 h, extruded at speed of 0.5 mm/s with extrusion ratio of 13, preheated at 360 °C for 2 h and rolled with a thickness ratio of 1.6 to produce sheet 50 mm in width along the transverse direction (TD), 1000 mm in length along the rolling direction (RD) and 5 mm in thickness. The analyzed composition was 2.13% Nd, 0.33% Zn, and Mg in balance, measured by inductively coupled plasma optical emission spectroscopy (ICP-OES).

2.2. Friction stir processing

Friction stir processing was conducted on a vertical milling machine. The concave-shaped shoulder diameter and pin length were 20 mm and ~2.3 mm, respectively. The pin diameter at the intersection of the shoulder was ~6.0 mm, and the tip of the pin was ~3.8 mm. The tool rotation rate, tool traverse speed, plunge depth and tool tilt were 400 rpm (FS-400 rpm) and 600 rpm (FS-600 rpm), 100 mm/min, ~1.5 mm, and 1.5°, respectively. The schematic of friction stir processing is presented in Fig. 1.

2.3. Microstructure characterization

The samples with dimensions of 10 mm × 10 mm × 3 mm were cut from the stir zone and then ground with SiC papers up to 2000 grit, ultrasonically cleaned in acetone, absolute ethanol, and distilled water sequentially, and finally dried. The microstructure was revealed by etching the polished surfaces of the alloy with an acetic-picral etchant (a mixture of 6 g picric-acid, 10 ml acetic-acid, 70 ml ethyl-alcohol and 10 ml distilled-water). Microstructural examinations on the as-rolled base alloy and the FSP specimens were conducted by both optical microscopy (OM) and scanning electron microscopy (SEM). The macro-texture was evaluated using an X-ray diffractometry (Bruker D8 ADVANCE).

2.4. Mechanical properties characterization

Vickers microhardness was measured on the process zone using a LECO semi-automatic indentation system at a load of 100 g for a dwell time of 10 s. Specimens for the tensile test of FSP and the base alloy were extracted using an electric discharge machine along the processing direction (PD). The I-shaped miniature tensile samples with a rectangular gauge cross-section possessed a gauge length of 15 mm, width of 2 mm, and thickness ranging within 1.8–2 mm. The surfaces and sides of the tensile specimens were ground using up to 2000 grit SiC papers to remove traces of cutting. The tensile tests were carried out on an Instron-5569 universal testing machine at a displacement rate of 1.0 mm/min and at ambient temperature. At least three specimens were tested for each condition and the elongation to failure was measured directly from the gauge marks made on the specimens.

Table 1
Chemical composition of Hank's solution (g/L).

NaCl	KCl	KH_2PO_4	$MgSO_4$	$NaHCO_3$	$CaCl_2$	Na_2HPO_4	Glucose
8.00	0.40	0.06	0.20	0.35	0.14	0.12	1.00

2.5. Corrosion evaluations

Corrosion behavior of NZ20 sheets and FSP specimens immersed in the Hank's solution at 37 °C was measured using mass loss, variation of pH, potentio-dynamic polarization curves and electrochemical impedance spectroscopy (EIS). The composition of Hank's solution is listed in Table 1. Samples for corrosion evaluations had dimensions of 10 mm × 10 mm × 2 mm, and were mechanically ground to 2000-grit finish with SiC papers.

Samples for potentiodynamic polarization curves were mounted in epoxy resin with an exposed surface area of 1 cm^2. Potentiodynamic polarization curves were measured using a PARSTAT 2263 potentiostat/galvanostat (Princeton Applied Research) workstation at a sweep rate of 0.5 mV s^{-1} after the specimen was held at the open circuit potential for 30 min to reach a steady state. EIS measurements were performed at the open circuit potential with a frequency range of 10^5–0.01 Hz A three-electrode electrochemical cell was used, with a platinum counter electrode, a saturated calomel reference electrode (SCE), and the NZ20 alloy sheet as the working electrode. The values of the corrosion current density (i_{corr}, in mA cm^{-2}) were converted to the corrosion rates P_i (mm/year), using the following [21,22]:

$$P_i = 22.85 i_{corr} \quad (1)$$

For each testing condition, three electrochemical tests were performed.

The mass loss was measured using immersion of 14 days. The ratio of sample surface area (cm^2) to solution volume (mL) was 1.25 for the immersion test. In order to keep the solution fresh, the solution was changed every day. After the immersion test, the corrosion products were removed using a cleaning solution containing 200 g L^{-1} CrO_3, 10 g L^{-1} $AgNO_3$ and 20 g L^{-1} $Ba(NO_3)_2$ for 1 min at room temperature. The mass loss data were converted to the corrosion rate, calculated using the following formula assuming a uniform corrosion rate [15]:

$$CR = \frac{KW}{ATD} \quad (2)$$

where CR is the corrosion rate (mm/year), K is a constant of 8.76×10^4, W is the mass loss (g), A is the surface area (cm^2), T is the time of immersion (h), and D is the density of the materials (g/cm^3).

The corrosion morphology of specimens was characterized using a scanning electron microscope and an optical camera. Topographic maps were obtained using a 3D measuring laser microscope. To ensure a high reproducibility, each corrosion test was conducted at least four times.

3. Results

3.1. Microstructures

Fig. 2 presents the microstructures of NZ20 before and after FSP. The microstructure of NZ20 sheet consisted of slightly elongated grains (Fig. 2(a)). The stir zone of FS-400 rpm was homogeneous and had much smaller grains with average size of about 2 μm (Fig. 2(c)). The microstructure of FS-600 rpm (Fig. 2(e)) revealed

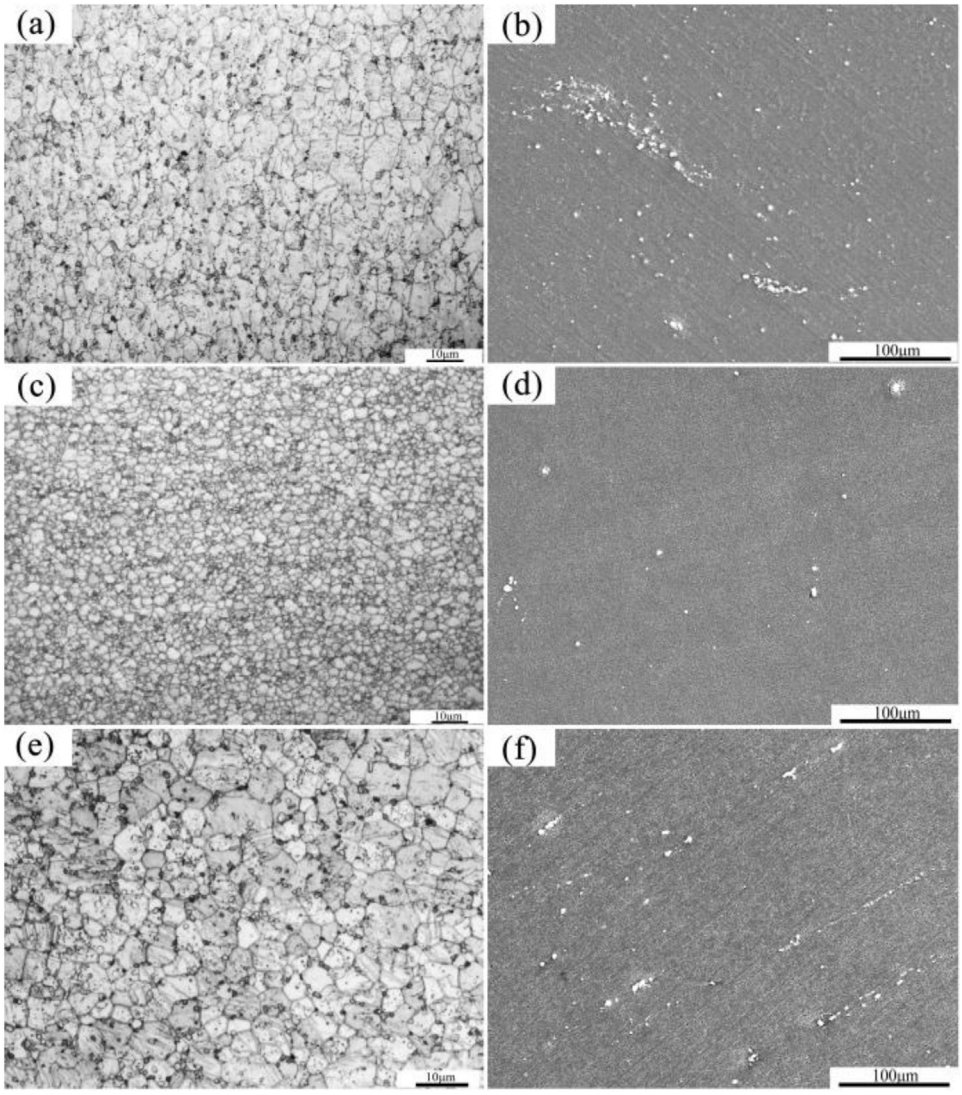

Fig. 2. Optical micrographs showing the microstructures of NZ20: (a) rolled sheet; (c) FS-400 rpm; (e) FS-600 rpm, and granular discrete second phases in SEM micrographs of NZ20: (b) rolled sheet; (d) FS-400 rpm; (f) FS-600 rpm.

Table 2
Grain size and volume fraction of second phases of NZ20 alloy.

Alloy state	Grain size	Volume fraction of second phase
Rolled sheet	~7μm	4.2 ± 0.2%
FS-400rpm	~2μm	0.2 ± 0.1%
FS-600rpm	~8μm	1.6 ± 0.1%

coarser and equiaxed grains, implying recrystalization during the FSP processing. There were many granular discrete second phases in the microstructure of NZ20 sheet (Fig. 2(b)), which were identified by EDS as the primary Mg-Nd-Zn precipitation particles [23]. There was a sharp decrease in the amount of second phases in FS-400 rpm (Fig. 2(d)). As the tool rotation rate was increased from 400 rpm to 600 rpm, there was a slight increase in the amount of second phases and semi-continuous phases along a certain direction (Fig. 2(f)). The grain size and volume fraction of second phases are listed in Table 2. Under mechanical stirring, some coarser second phases were broken into smaller size particles. Re-distribution of second phases was affected by a number of factors including the metal flow during FSP, heat generation, tool material and design. At a lower speed of rotation, the zone around the pin had less heavy metal flow with higher cooling rate, which inhibited second phase precipitation.

Fig. 3 presents the (0001) pole figures for NZ20 before and after FSP. The *c* axis was tilted toward PD-TD surface at a certain angle, and each sample exhibited a general basal texture. The intensity of different texture components suggests that the dominant plastic deformation mode is <*a*> slip, while the deformation in the <*c*> direction is minor. This result is in a good agreement with the present understanding of deformation mechanisms in magnesium alloys. The texture intensity varied in the three different conditions. The FS-400 rpm produced a stronger basal texture.

3.2. Mechanical properties

The mechanical properties of NZ20 are summarized in Table 3 and Fig. 4. The ultimate tensile strength (UTS) and elongation of NZ20 rolled sheet were 258 MPa and 10%, respectively. The FSPed alloy showed significantly higher elongation, but lower hardness and strength, which decreased with increasing rotation rate.

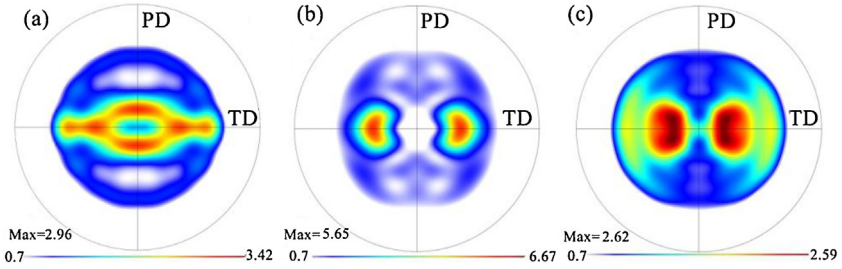

Fig. 3. (0001) pole figures of NZ20: (a) rolled sheet; (b) FS-400 rpm; (c) FS-600 rpm.

Table 3
Mechanical properties of NZ20 alloy.

Alloy state	UTS (MPa)	YS (MPa)	Elongation (%)
Rolled sheetFS-400 rpmFS-600 rpm	258 ± 12150 ± 583 ± 2	220 ± 862 ± 433 ± 3	10.6 ± 1.327.3 ± 2.423.5 ± 1.2

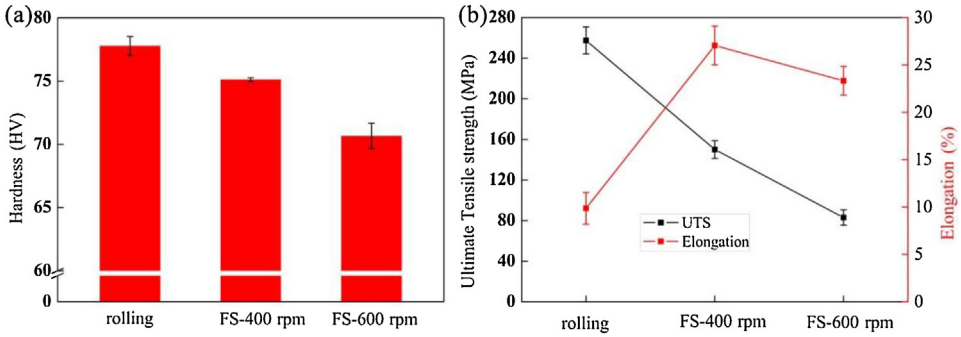

Fig. 4. Hardness (a) and UTS (b) and elongation of NZ20 before and after FSP.

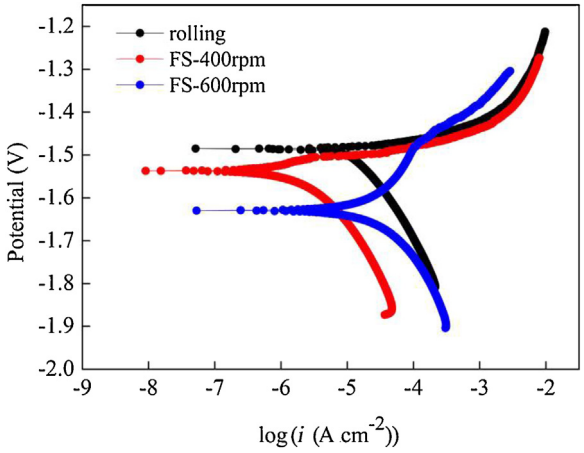

Fig. 5. Polarization curves in Hank's solution of NZ20 before and after FSP.

Table 4
Electrochemical data for NZ20 in Hank's solution derived from the polarization curves.

Alloy state	E_{corr} (V)	i_{corr} ($\times 10^{-6}$ A cm^{-2})	CR (mm year^{-1})
Rolled sheet	−1.49 ± 0.12	14.0 ± 0.2	24.8 ± 0.2
FS-400 rpm	−1.54 ± 0.04	2.6 ± 0.06	4.6 ± 0.09
FS-600 rpm	−1.63 ± 0.03	31.6 ± 0.4	56 ± 3

3.3. Electrochemical behavior

Fig. 5 presents the potentiodynamic polarization curves in Hank's solution for NZ20 before and after FSP. Table 4 presents the values obtained from the potentio-dynamic polarization curves. The cathodic polarization branches represent the cathodic hydrogen evolution, and anodic polarization branches represent the dissolution of Mg. The i_{corr} value decreased in the following order: FS-600 rpm, as-rolled and FS-400 rpm. The corrosion rate, P_i, decreased in the same order: FS-600 rpm, as-rolled and FS-400 rpm.

The AC impedance spectra in Fig. 6 show single capacitive loops in the measured frequency range. The diameter of the capacitive loop is associated with the polarization resistance. The loop diameter for FS-400 rpm was the largest, signifying that the electrochemical process is the slowest. In the case of Bode plots of $|Z|$ (modulus of impedance) with frequency, the impedance values increased with decreasing frequency for two samples whilst FS-400 rpm exhibited a higher |Z| value, suggesting a higher corrosion resistance for FS-400 rpm. The equivalent circuit, illustrated in Fig. 6(d), was used to analyze the Nyquist spectra and the fitted parameters are listed in Table 5. R_s, R_{ct} and R_f represent the solution resistance, charge-transfer resistance and film resistance, respectively. Constant phase elements CPE_{ct} and CPE_f were used to describe the capacitive behaviors of charge-transfer (C_{ct}) and oxide film (C_f) due to the dispersion effect. Q is a CPE constant, and n is a dimensionless CPE index. The values of R_{ct} and R_f in Table 5 were higher for FS-400 rpm, implying higher corrosion resistance.

3.4. Immersion performance

Fig. 7 shows the pH variation of the Hank's solution for NZ20 as a function of immersion time. In the early stage of corrosion, pH of the solution increased because of the formation of $Mg(OH)_2$ precipitate, inferring the corrosion status from the height of pH value. During the 14 days, the pH of FS-400 rpm specimen was lowered slightly and the pH of the other two samples remained higher. Fig. 7(b) presents the corrosion rates derived from mass loss for the NZ20

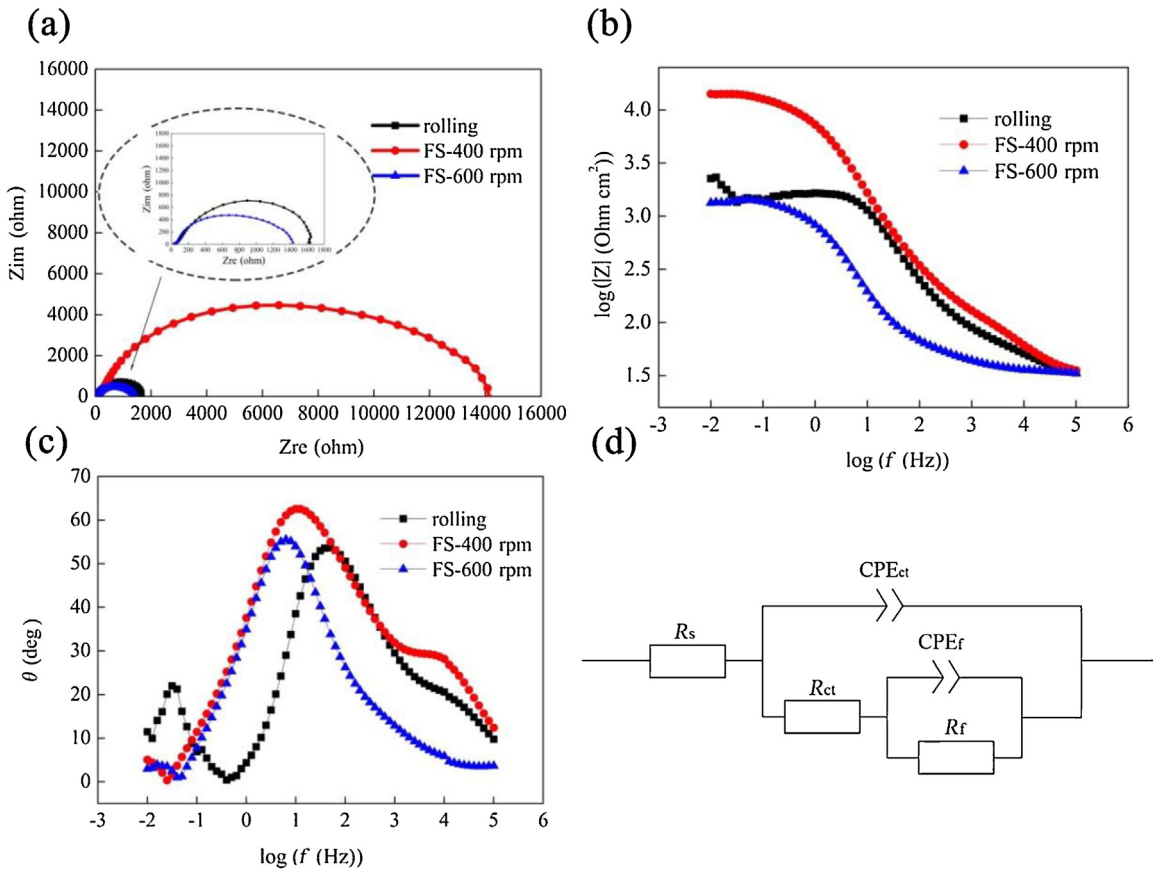

Fig. 6. EIS spectra of NZ20 before and after FSP in Hank's solution: (a) Nyquist plot; (b) Bode plots of |*Z*| with frequency; (c) Bode plots of phase angle with frequency; (d) equivalent circuit of EIS spectra.

Table 5
Fitting electrochemical parameters of EIS.

Alloy state	R_s (Ω cm^2)			R_{ct} (Ω cm^2)			CPE$_{ct}$			R_f (kΩ cm^2)			CPE$_f$			
							Q_{ct} (μF s^n cm^{-2})			n			Q_f (μF s^n cm^{-2})			n
RollingFS-400rpmFS-600rpm	31.91	30.8	34.04	71.7	166.5	43.88	7.27	10.77	9.18	0.760.700.74	1.67	13.75	1.33	1.34	13.00	9.31	0.860.820.88

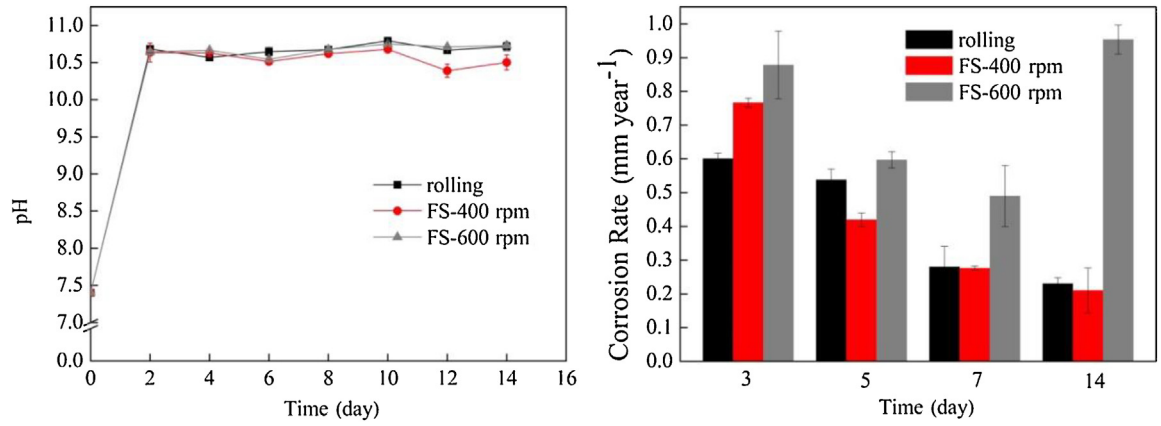

Fig. 7. pH evolution (a) and corrosion rate (b) of NZ20 before and after FSP immersed in Hank's solution for 14 days.

before and after FSP immersed in Hank's solution for 14 days. The corrosion rate for three NZ20 conditions decreased in the following order: FS-600 rpm, as-rolled and FS-400 rpm. The FS-400 rpm had the lowest corrosion rate, especially during a long time immersion. This ranking of the corrosion rate was consistent with that from the potentio-dynamic polarization curves. Nevertheless there was slightly different for the numerical values.

Fig. 8 presents typical corrosion morphologies of NZ20 before and after FSP after removing the corrosion products at the 7th day. The magnitude of corrosion attack was different for the three

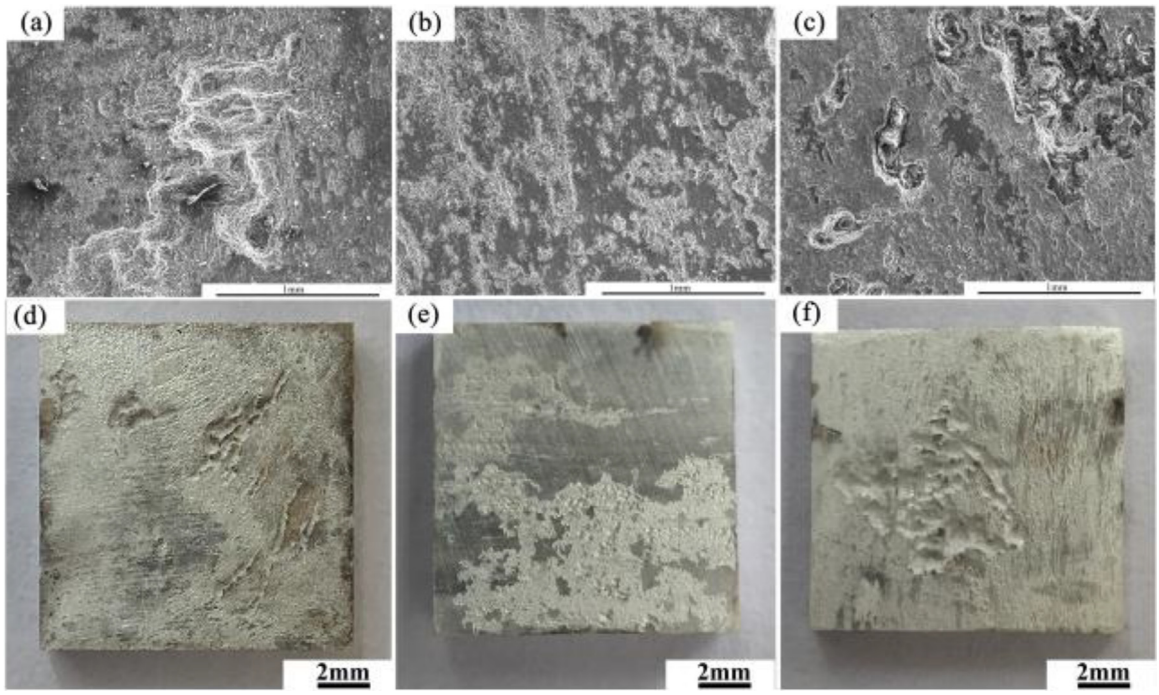

Fig. 8. SEM images of the corrosion surfaces of NZ20 after removing corrosion products: (a) rolled sheet; (b) FS-400 rpm; (c) FS-600 rpm, and macro corrosion morphologies of NZ20 before and after FSP, (d) rolled sheet; (e) FS-400 rpm; (f) FS-600 rpm.

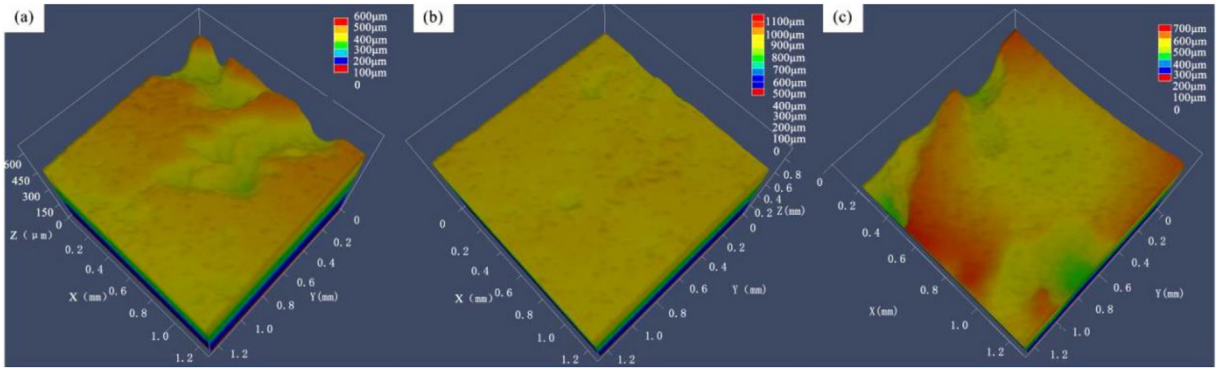

Fig. 9. Topographic map of NZ20 alloy before and after FSP: (a) rolled sheet; (b) FS-400 rpm; (c) FS-600 rpm.

conditions. Corrosion pits on the surface of FS-400 rpm were shallower and more uniform than that for the two other conditions. FS-600 rpm had some local severe corrosion pits.

Fig. 9 shows the topographic map of NZ20 before and after FSP immersed for 7 days. There were more flat surfaces on FS-400 rpm and the depth of corrosion pits reached to ~200 μm in the local position for the un-processed alloy, which was in agreement with the results of the corrosion morphology by SEM.

4. Discussion

As stated above, there were obvious changes in grain size and crystallographic texture of the rolled NZ20 sheets after friction stir processing. These factors, i.e., grain size, texture and second phase, determine the corrosion rate of NZ20 alloy.

4.1. Effect of grain size

Friction stir processing substantially decreased the grain size of NZ20 at a rotating speed of 400 rpm, which implied the occurrence of complete dynamic recrystallization (DRX) during FSP. The severe plastic deformation induced during FSP resulted in breaking down of the initial structure and created a large number of low angle grain boundaries and misoriented subgrains, and favored places for recrystallization nucleation [24]. Previous research on the influence of grain size on corrosion behavior of Mg alloys [25,26] have suggested that grain boundaries act as a corrosion barrier to retard the corrosion progress. In this study, FS-400 rpm with finer and homogeneous grains had a lower corrosion rate, which supports the hypothesis that grain boundaries act as a corrosion barrier. In addition, the grain refinement can reduce the mismatch stress between the surface layer and magnesium substrate as well as pitting initiation. The relation between the grain size and polarization resistance approximately follows the Hall-Petch equation [27].

4.2. Effect of texture

Texture is another important micro-structural characteristic of Mg alloys. Previous research relating grain orientation and corrosion performance of Mg alloys [28–30] has indicated that the corrosion rate has been correlated to the surface energy [31], and crystallographic planes contribute largely to the surface energy.

For pure Mg, the (0001) plane has the highest atomic density (1.13×10^{19} atoms/m^2), followed by the (11 $\bar{2}$ 0) plane (6.94×10^{18} atoms/m^2) and then the (10 $\bar{1}$ 0) plane (5.99×10^{18} atoms/m^2) [32]. Higher atomic coordination is associated with a more-closely packed plane, with a higher binding energy and a lower surface energy, and a higher activation energy for dissolution. The electrochemical dissolution rate of a metal can be expressed by [33]:

$$Ia = nFkexp\left(\frac{-Q + \alpha nFE}{RT}\right) \quad (3)$$

where n is the number of electrons involved in the electrochemical reaction; k is a reaction constant; F, R, T and E are Faraday constant, gas constant, absolute temperature and electrode potential, respectively. α is a transit coefficient. Q is the activation energy for a metallic ion to escape from the metal lattice and dissolve into the solution. The activation energy for dissolution of a densely packed surface is higher than that for a loosely packed surface. Therefore, the (0001) plane has the lowest corrosion rate among all the planes of Mg [34,35]. The basal texture intensity of FS-400 rpm was much higher than for the rolled sheet and FS-600 rpm, which indicates that FS-400 rpm contained a higher fraction of (0001) oriented grains and thus explains the lowest corrosion rate of FS-400 rpm.

4.3. Effect of second phases

The second phase is also a key factor determining the corrosion behavior for Mg alloys. The second phases typically accelerate the corrosion rate of Mg alloys [36–38], because they usually act as a cathode to accelerate the corrosion. In the stir zone, severe mechanical rotation around the pin could break the coarser second phase particles into finely-divided ones and the friction heat could also dissolve more second phases into the matrix. Hence the local dispersed mirco-galvanic could cause more homogeneous corrosion. The processed structure with large number of nano-sized second phase particles precipitated in the grain interiors without precipitation of the second phase at grain boundaries results in more uniform corrosion with respect to the sample with continuous second phase placed at grain boundaries and macro-sized second-phase particles within the grain.

5. Conclusions

The microstructure was evaluated before and after the severe plastic deformation of FSP in terms of the grain size, crystallographic texture and amount of second phase of the rolled NZ20 sheet, and was related to the corrosion behavior. The following conclusions can be made:

(1) Appropriate FSP led to grain refinement, stronger basal texture and a considerably higher elongation for NZ20.
(2) The corrosion rate of NZ20 in Hank's solution decreased in the following order: FS-600 rpm > rolled sheet > FS-400 rpm, indicating that FS-400 rpm had the lowest corrosion rate.
(3) The effect of friction stir processed microstructure on decreasing the corrosion rate of NZ20 alloy can be attributed to grain refinement, a stronger basal texture and a smaller amount of second phase particles.

Acknowledgements

This work was finnacially supported by the Chinese Natural Science Foundation (No. 51874368), the Key Program of China on Biomedical Materials Research and Tissue and Organ Replacement (Nos. 2016YFC1101804 and 2016YFC1100604), and Institute of Metal Research, Chinese Academy of Sciences (No. 2015-ZD01).

References

[1] R.C. Zeng, X.T. Li, L.J. Liu, S.Q. Li, F. Zhang, J. Mater. Sci. Technol. 32 (2016) 437–444.
[2] C. Wang, H.T. Yang, X. Li, Y.F. Zheng, J. Mater. Sci. Technol. 32 (2016) 909–918.
[3] R.C. Zeng, L. Wang, D.F. Zhang, H.Z. Cui, E.H. Han, Front. Mater. Sci. 8 (2014) 230–243.
[4] R.C. Zeng, W. Qi, F. Zhang, H. Cui, Y. Zheng, Prog. Nat. Sci. 24 (2014) 492–499.
[5] N. Li, Y.F. Zheng, J. Mater. Sci. Technol. 29 (2013) 489–502.
[6] K. Chiu, M. Wong, F. Cheng, H. Man, Surf. Coat. Technol. 202 (2007) 590–608.
[7] L.Y. Li, L.Y. Cui, R.C. Zeng, S.Q. Li, X.B. Chen, Y.F. Zheng, M.B. Kannan, Acta Biomater. 79 (2018) 23–36.
[8] L.L. Tan, Q. Wang, X. Lin, P. Wan, G.D. Zhang, Q. Zhang, K. Yang, Acta Biomater. 10 (2014) 2333–2340.
[9] L. Guo, W. Wu, Y. Zhou, F. Zhang, R. Zeng, J. Zeng, J. Mater. Sci. Technol. 34 (2018) 1455–1466.
[10] Y. Song, E.H. Han, D. Shan, D.Y. Chang, B.S. You, Corros. Sci. 65 (2012) 322–330.
[11] M.C. Zhao, M. Liu, G.L. Song, A. Atrens, Corros. Sci. 50 (2008) 3168–3178.
[12] M.C. Zhao, M. Liu, G.L. Song, A. Atrens, Adv. Eng. Mater. 10 (2008) 93–103.
[13] N.N. Aung, W. Zhou, Corros. Sci. 52 (2010) 589–594.
[14] N. Birbilis, K.D. Ralston, S. Virtanen, H.L. Fraser, C.H.J. Davies, Br. Corros. J. 45 (2010) 224–230.
[15] G.R. Argade, S.K. Panigrahi, R.S. Mishra, Corros. Sci. 58 (2012) 145–151.
[16] M. Alvarez-Lopez, M.D. Pereda, J.A.D. Valle, M. Fernandez-Lorenzo, M.C. Garcia-Alonso, O.A. Ruano, Acta Biomater. 6 (2010) 1763–1771.
[17] R.C. Zeng, J. Chen, W. Dietzel, R. Zettler, J.F.D. Santos, M.L. Nascimento, K.U. Kainer, Corros. Sci. 51 (2009) 1738–1746.
[18] N. Kumar, R.S. Mishra, N.B. Dahotre, R.E. Brennan, K.J. Doherty, K.C. Cho, Mater. Des. 110 (2016) 663–675.
[19] H.S. Arora, H. Singh, B.K. Dhindaw, Corrosion 69 (2013) 122–135.
[20] G.R. Argade, K. Kandasamy, S.K. Panigrahi, R.S. Mishra, Corros. Sci. 58 (2012) 321–326.
[21] M.C. Zhao, M. Liu, G.L. Song, A. Atrens, Adv. Eng. Mater. 10 (2008) 104–111.
[22] M.C. Zhao, P. Schmutz, S. Brunner, M. Liu, G.L. Song, A. Atrens, Corros. Sci. 51 (2009) 1277–1292.
[23] J. Li, L. Tan, P. Wan, X. Yu, K. Yang, Mater. Sci. Eng. C-Mater. 49 (2015) 422–429.
[24] T. Zhang, Y. Shao, G. Meng, Z. Cui, F. Wang, Corros. Sci. 53 (2011) 1960–1968.
[25] R. Zeng, K.U. Kainer, C. Blawert, W. Dietzel, J. Alloy. Compd. 509 (2011) 4462–4469.
[26] R.C. Zeng, L. Sun, Y.F. Zheng, H.Z. Cui, E.H. Han, Corros. Sci. 79 (2014) 69–82.
[27] W. Yuan, S.K. Panigrahi, J.Q. Su, R.S, Scr. Mater. 65 (2011) 994–997.
[28] M. Liu, M. Qiu, M.C. Zhao, G. Song, A. Atrens, Scr. Mater. 58 (2008) 421–424.
[29] K.S. Shin, M.Z. Bian, N.D. Nam, JOM 64 (2012) 664–670.
[30] L.G. Bland, K. Gusieva, J.R. Scully, Electrochim. Acta 227 (2017) 136–151.
[31] G.L. Song, Z. Xu, Corros. Sci. 54 (2012) 97–105.
[32] M. Liu, P.L. Uggowitzer, P. Schmutz, A. Atren, JOM 60 (2018) 39–44.
[33] G.L. Song, R. Mishra, Z.Q. Xu, Electrochem. Commun. 12 (2010) 1009–1012.
[34] Z. Pu, G.L. Song, S. Yang, J.C. Outeiro, O.W.D Jr, D.A. Puleo, Corros. Sci. 57 (2012) 192–201.
[35] A. Atrens, G.L. Song, M. Liu, Z. Shi, F. Cao, M.S. Dargusch, Adv. Eng. Mater. 17 (2015) 400–453.
[36] M.C. Zhao, Y.L. Deng, X.M. Zhang, Scr. Mater. 58 (2008) 560–563.
[37] Y.C. Zhao, M.C. Zhao, R. Xu, L. Liu, J.X. Tao, C. Gao, C. Shuai, A. Atrens, J. Alloy. Compd. 770 (2019) 549–558.
[38] M.C. Zhao, M. Liu, G.L. Song, A. Atrens, Corros. Sci. 50 (2008) 1939–1953.